ORIGINAL RESEARCH ARTICLE

Conventional *vs.* Temperature-Gradient Transient Liquid Phase Bonding of Stainless Steel 304 Using a Multi-component (Fe–Ni–Mo–B) Filler Metal

FARZIN JABBARI and ALIAKBAR EKRAMI

The application of the multi-component Fe-based filler metals (FMs) for transient liquid phase (TLP) bonding of AISI 304 austenitic stainless steel has been overshadowed by dissimilar interlayers merely due to their shorter isothermal solidification time. However, the latter usually suffers from low efficiency in terms of mechanical properties even after homogenization of heat treatment. This study shows that by imposing a temperature gradient across the bond line during the TLP bonding process (TG-TLP), it is possible to reduce the isothermal solidification time significantly. This renews the interest in utilizing multi-component Fe-based FMs. In this regard, the TG-TLP bonding process was carried out on the AISI 304/Fe–Ni–Mo–B/AISI 304 system at different holding times and compared to those of the conventional TLP (C-TLP) bonding case. Results revealed that the TG-TLP bonding scenario benefits from a fast isothermal solidification, making that the implementation of the multi-component Fe-based FMs is cost and time effective. Moreover, the absence of the boride precipitates in the diffusion-affected zone (DAZ) of the base material (BM), along with the formation of a joint region with a chemical composition comparable to that of the BM, eliminates the need for homogenization post-processing. These features of the TG-TLP bonding process, in tandem with a non-planar interface, led to a joint with shear strength efficiency of 100 pct fractured from the BM. The lessons learned from the explored fast isothermal solidification mechanism and lack of boride formation phenomenon in the DAZ can also be applied to the TG-TLP bonding of other steels and Ni-based superalloys.

FARZIN JABBARI and ALIAKBAR EKRAMI are with the Department of Materials Science and Engineering, Sharif University of Technology, 11365-9466 Tehran, Iran. Contact e-mail: F.Jabbari94@sharif.edu

Manuscript submitted January 29, 2022; accepted August 14, 2022.
Article published online September 21, 2022

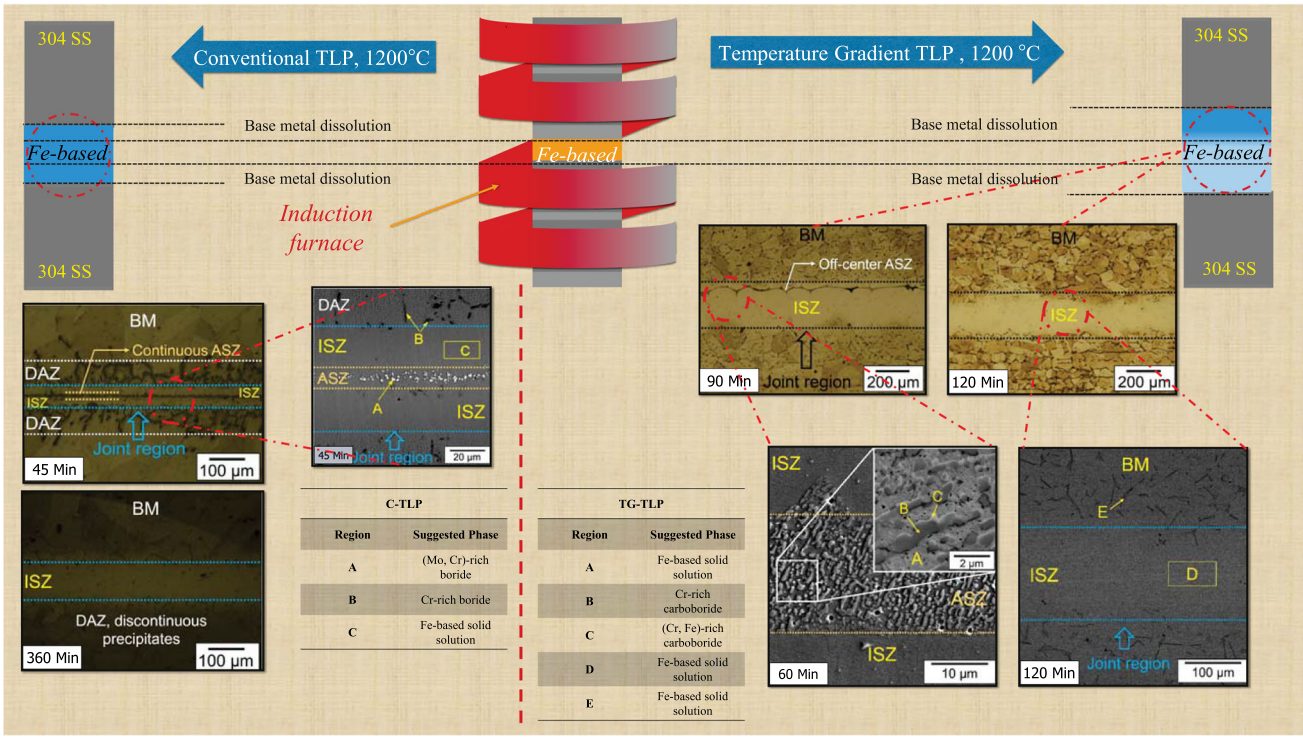

https://doi.org/10.1007/s11661-022-06817-9

I. INTRODUCTION

TRANSIENT liquid-phase (TLP) bonding is one of the most promising joining techniques which has revolutionized the heat exchanger, aerospace, and turbine industries by offering the possibility of creating plate-fin heat exchangers, lattice structures, and honeycomb panels with an efficiency approaching 100 pct in terms of mechanical properties.[1–6] Having the same concept as that of the brazing, the TLP bonding process benefits from a low-melting point filler metal (FM) containing one or multiple-melting point depressant (MPD) elements.[7–10] The major difference between the brazing and the TLP bonding process is the incomplete depletion of the MPD atoms from the liquid phase in the latter due to the shorter bonding cycles. This results in the athermal solidification of the majority of the liquid phase—a fertile ground for the formation of brittle intermetallic and eutectic phases.[11–13] In the TLP bonding process, on the other hand, the complete isothermal solidification of the liquid phase with a mechanism thoroughly explained in References 14 through 17 can avert the formation of such phases in the joint region. Accordingly, the TLP-bonded joints possess higher corrosion resistance and fracture toughness.[18,19]

In many of the applications in the abovementioned industries, austenitic stainless steels are the potential nominates owing to their outstanding corrosion resistance, high-temperature strength, and thermal fatigue properties.[20] For instance, AISI 304 stainless steel has found its way into various applications, including heat exchangers.[21] Since the solid state or fusion welding of the topologically complex-structured AISI 304 stainless steel heat exchangers is impossible,[22] their TLP bonding processability needs to be studied. While other joining techniques like brazing can also be considered for heat exchanger fabrication,[23] the penalties associated with the formation of brittle eutectic micro-constituents in the joint region tip the balance in favor of the TLP bonding process.[3,24] Although other manufacturing techniques such as laser powder bed fusion additive manufacturing can also be implemented to fabricate these heat exchangers,[25–27] they are still cost prohibitive, especially for mass production and large-sized components.[22] Therefore, it is fair to conclude that the TLP bonding process is the best option for fabricating the heat exchangers. The same statement would be valid for many other applications.

Several attempts have been made in the recent decade to achieve ideal similar/dissimilar AISI 304 joints having a strength greater or comparable to that of the BM. However, none of them was reported to be successful in the as-weld condition or even after homogenization heat treatment. Kazazi and Ekrami[28] investigated the TLP bonding of AISI 304 by utilizing a Ni-based FM. They reported that the average shear strength of the joint after the homogenization stage was 83 pct of that of the BM. Sadeghian *et al.*[29] used Co-based FM to bond AISI 304 stainless steel. The shear strength of the joint in the

as-weld condition when isothermal solidification was accomplished was ~ 50 pct of that of the BM. They could increase it to 72 pct by applying a homogenization heat treatment. Finally, Mohammadi and Ekrami[30] evaluated the dissimilar TLP joint of AISI 304 stainless steel and dual-phase steel with the Cu interlayer under a temperature gradient. They found that the shear strength of the homogenized joint was higher than that of the dual-phase steel; nevertheless, it was ~ 80 pct of the AISI 304 stainless steel.

The main reason for the inability to obtain an ideal joint is that the FMs employed in different research studies in the literature are dissimilar to the BM in terms of chemical composition.[31,32] For instance, pure Cu, Ni-based, or Co-based FMs are implemented in many abovementioned studies. That is why they failed to create an ideal joint whose strength is at least comparable to that of the BM in the as-weld condition. Moreover, even when the Fe-based FMs were used, they were usually binary systems that suffered from the lack of strengthening alloying elements.[33] Therefore, a logical approach to resolve the mentioned problem is implementing Fe-based multi-component FMs. On this account, a Fe–Ni–Mo–B interlayer is used in this study to understand whether the presence of Mo- and Ni-alloying elements can ensure a high-strength corrosion-resistant joint. The B element in this FM acts as the MPD element to reduce the melting temperature of the FM to be able to perform the TLP bonding process at temperatures lower than the solidus temperature of the AISI 304 stainless steel.[31]

Regardless of the fact that a few Fe-based multi-component FMs are commercially available, their efficiency in producing an ideal joint has not been investigated for many stainless steels, including AISI 304. According to some research studies conducted on the TLP bonding process of steels and Ni-based superalloys, multi-component FMs[11,31,34,35] are not attractive for industrial applications because of their long isothermal solidification time. To make them less repelling for industrial applications, temperature-gradient liquid-phase bonding (TG-TLP) can be a suitable substitution. TG-TLP bonding process is a novel approach for joining advanced materials based on imposing a temperature gradient across the bond line. This has been shown to promote the unidirectional movement of both solid/liquid interfaces from the cooler to the hotter side.[36–38] As opposed to the conventional TLP (C-TLP) bonding process, in which diffusion only occurs from the liquid phase toward the solid phase (based on the classical definition), the TG-TLP bonding process benefits from the diffusion of MPD atoms along with other involving elements within the liquid phase as well.[39,40] This can affect the isothermal solidification time. Depending on the BM and FM chemical composition, as well as the bonding temperature and the applying temperature gradient, this change in the diffusion may decrease the isothermal solidification time.[41,42]

This research study focuses on the C-TLP and TG-TLP bonding of AISI 304 stainless steel using a Fe-based multi-component FM to investigate the feasibility of achieving an ideal joint in terms of mechanical properties. The effect of bonding time on microstructural evolutions was thoroughly investigated. The isothermal solidification accomplishment time was found in both C-TLP and TG-TLP cases to find the optimum-bonding process from the processing time perspective. Implications of the findings in this study are also essential for other steels, Ni-based, and Co-based superalloys with a high amount of alloying elements.

II. EXPERIMENTAL PROCEDURE

In this study, a wrought AISI 304 stainless steel sheet with a nominal thickness of 6 mm was used as the BM. The chemical composition of the BM was confirmed by the spark emission spectroscopy, shown in Table I. TLP bonding test coupons with the dimensions of 12 × 12 × 6 mm^3 were cut out of the parent sheet. The faying surfaces of the test coupons were ground and ultrasonically cleaned prior to the bonding. They were kept in alcohol to hinder any possible oxidation and/or contamination. An iron-based (Fe–Ni–Mo–B) FM with a nominal thickness of 40 μm and a nominal chemical composition provided in Table I was utilized to create the liquid phase during the TLP bonding process. The FM was placed between two pieces of test coupons, and the assembled BM/FM/BM sandwich (Figure 1(a)) was fixed by a stainless steel fixture exerting a uniaxial pressure of 0.2 MPa to the sandwich system.

C-TLP bonding process was performed in a high-temperature silicon carbide element box furnace. The TG-TLP bonding process, on the other hand, was conducted in an induction furnace. This was achieved by maintaining the sandwich system in the off-center of the coil but at its axis of symmetry, as this results in asymmetrical heating. While testing different holding times (Table II), the fixed bonding temperature of 1200 °C was selected for both C-TLP and TG-TLP bonding processes to ensure the melting of the FM but not the BM. No protective atmosphere or vacuum condition was applied for both TLP bonding processes. All samples were air cooled after the TLP bonding process.

The bonding temperature was selected based on the rule that it should not be too high to cause detrimental influence on the BM and should not be too low to result

Table I. Chemical Composition (in Wt Pct) of the AISI 304 Stainless Steel and Fe-Based FM

Sample/Element	Fe	Ni	Cr	Mo	Mn	Si	C	B	P + S
AISI 304	bal	8.25	18.36	—	1.05	0.55	0.013	—	< 0.34
Filler Metal	bal	44.23	—	7.61	—	—	—	3.86	—

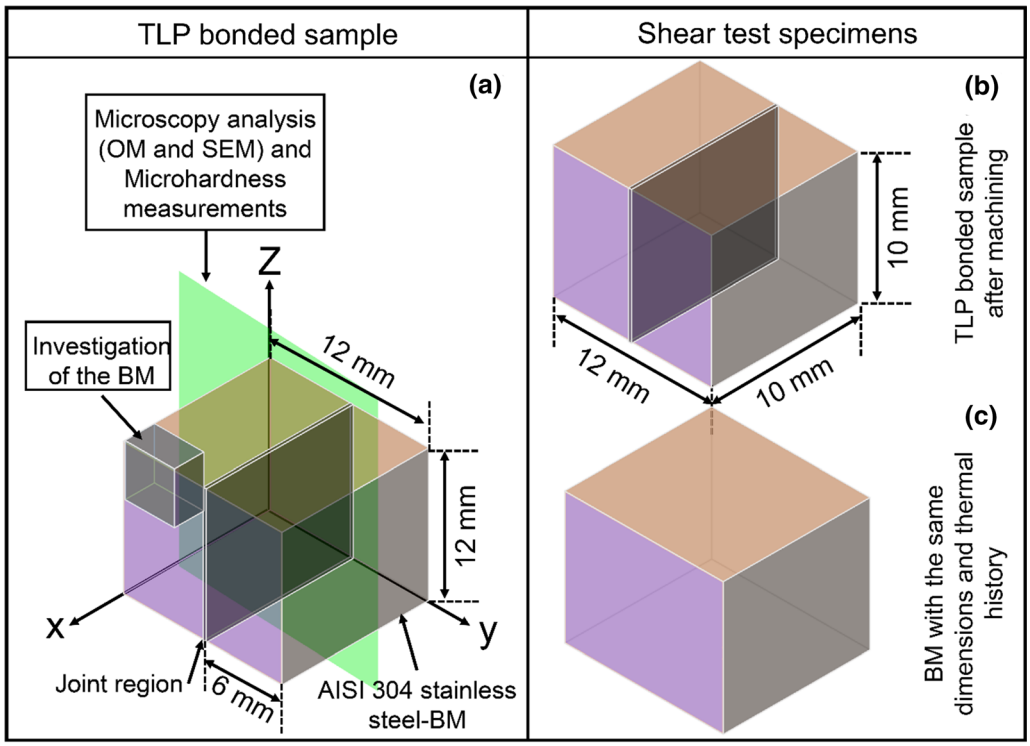

Fig. 1—Schematic illustration of (*a*) TLP-bonded samples, (*b*) and (*c*) the TLP-bonded and BM shear test specimens which experienced the same thermal history. The cross section at which the OM, SEM, and microhardness measurements were performed on the TLP-bonded samples and BM is shown in (a).

Table II. Details of the Thermal Cycles Applied to the C-TLP and TG-TLP Bonded Samples

Bonding Process	Bonding Temperature (°C)	Holding Time (Minutes)	Cooling Strategy
C-TLP	1200	45, 120, 240, 360	air cooled
TG-TLP		60, 90, 120	

in slow diffusion of the MPD atoms or prolonged isothermal solidification completion time. According to the literature, temperatures higher than 1200 °C lead to the formation of detrimental phases in AISI 304 stainless steel.[43] That is why the bonding temperature of 1200 °C was selected to ensure a high isothermal solidification rate without being concerned about any detrimental effect on the BM. Regarding the selected bonding times, the purpose was to find the isothermal solidification completion time with a few trials. Therefore, it does not matter if the soaking times and time steps are different in the C-TLP and TG-TLP bonding processes. In the TG-TLP bonding process, the temperature gradient is built by the induction furnace. Thus, the temperature gradient could not be measured experimentally. Moreover, the temperature gradient changes with the relative position of the sample and induction coil. Also, the temperature gradients at the edge and center of the bonding area are different, which are related to the intrinsic of induction heating. The criterion in selecting the temperature gradient (position of the sample in the induction furnace) was the formation of the non-planar BM/joint interface. In other words, pilot testing was exercised by putting the samples in different positions. Then, the samples were sectioned, and their interface was observed by optical microscopy (OM). Finally, one of the samples with a sinusoidal interface was used for the rest of the studies. The magnitude of the temperature gradient (G) of the selected sample was calculated using the following formula[36]:

$$t_b = W_0 \Phi D G, \quad [1]$$

where W_0, D, and t_b denote the initial thickness of the FM, the solute (B) diffusivity in the liquid layer, and the isothermal solidification completion time. The term Φ was calculated using the following equation[41]:

$$\Phi = -m_l C_{l0} \left(\frac{1}{K} - 1 \right), \quad [2]$$

in which m_l, C_{l0}, and K are the slope of the liquidus line, the equilibrium concentration of MPD in the liquid

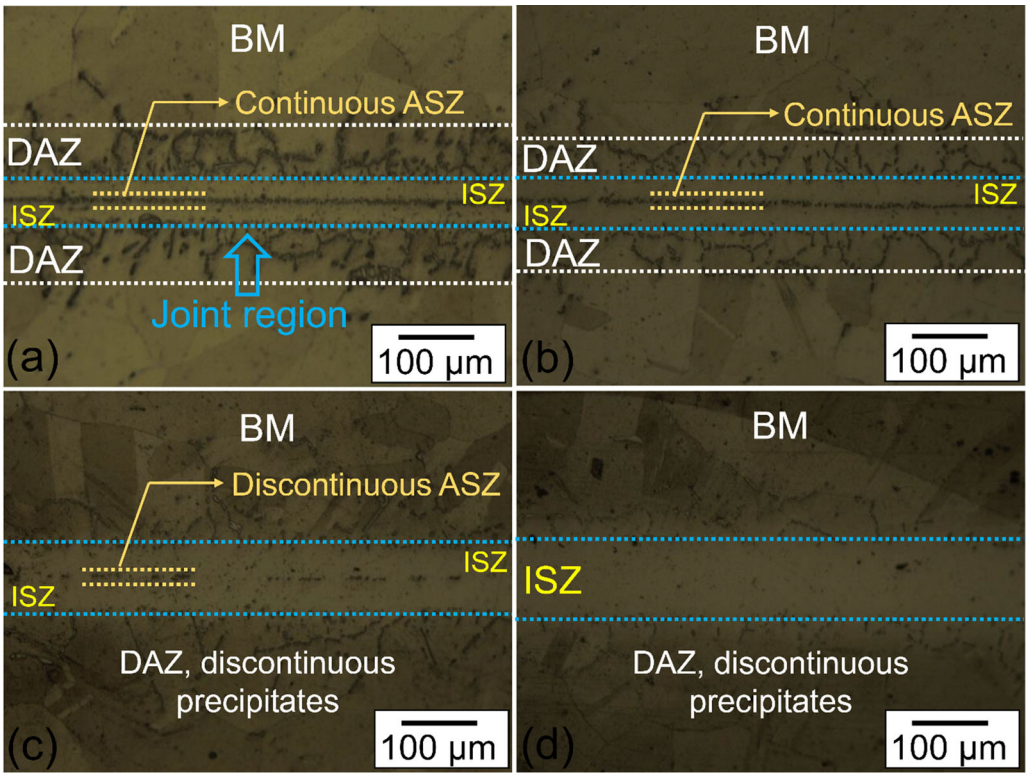

Fig. 2—Optical micrographs of C-TLP-bonded samples at 1200 °C for bonding times of (*a*) 45, (*b*) 120, (*c*) 240, and (*d*) 360 minutes.

layer at the bonding temperature, and the equilibrium partition coefficient, respectively. The m_l, C_{l0}, and K values for the AISI 304 stainless steel/Fe–Ni–Mo–B/AISI 304 stainless steel system were estimated from the Fe–B binary phase diagram shown in Section IV–B. The magnitude of D for the diffusion of B in the multi-component liquid layer was estimated from the diffusion of C in pure molten iron and was set to be 0.79 m^2/s.[44] By knowing t_b, W_0, and the above variables, G was found to be 0.6 K/mm.

The bonded samples were sectioned (Figure 1(a)), ground, and polished according to the standard metallographic procedure. AISI 304 stainless steel was etched with an etchant having 50 mL HCl, 25 mL H_2O, 15 g $FeCl_3$, and 3 g NH_4Cl. The joint microstructure was studied by OM, Olympus BX51m, and Tescan Mira-3 field emission scanning electron microscopy (FESEM) equipped with an energy dispersive spectrometer (EDS). Grain size measurement was performed as per ASTM E112 standard.

Microhardness test was carried out by a Leitz-300 series microhardness tester across the joint region (Figure 1(a)) of the bonded samples as per ASTM E384-16 standard, using a 100 g load and dwell time of 15 seconds. Shear test was used to assess the strength of the optimum TLP-bonded sample and the BM (Figure 1(b)). The BM was tested after experiencing a thermal cycle identical to that of the bonded sample (Figure 1(c)). The test was conducted on a Hounsfield Santam tensile machine with a cross-head speed of 1 mm/min. The TLP-bonded samples were machined to 10 × 10 × 12 mm^3 prior to the test to remove any possible filets at the edges (Figure 1(b)). The bonded samples were sheared at the 10 × 10 mm^2 cross section. Regarding the machining of the shear test specimens, wire EDM machining was used to ensure that no significant stresses were generated. After wire EDM machining, the surface of the specimens was ground to eliminate any possible scratches and weak points. Three shear test specimens were prepared and tested to ensure the repeatability of the obtained data. The shear strength value reported in the manuscript is the average of three measurements. Fractured surfaces and crack propagation paths were assessed by FESEM and OM.

III. RESULTS

A. *Microstructural Evolutions During C-TLP*

The optical micrographs in Figures 2(a) through (d) illustrate the microstructure of the joint region in C-TLP-bonded samples at 1200 °C for 45, 120, 240, and 360 minutes, respectively. As is evident in Figure 2(a), the microstructure of the joint region can be divided into four distinct zones: (i) isothermal solidification zone (ISZ), (ii) athermal solidification zone (ASZ), (iii) diffusion-affected zone (DAZ), and (iv) BM. The formation of the ISZ is caused by the diffusion of B atoms from the molten FM into the solid BM during the holding time at the bonding temperature. The driving force behind such a diffusion after achieving an equilibrium condition at the solid/liquid (S/L) interface during the dissolution stage is the

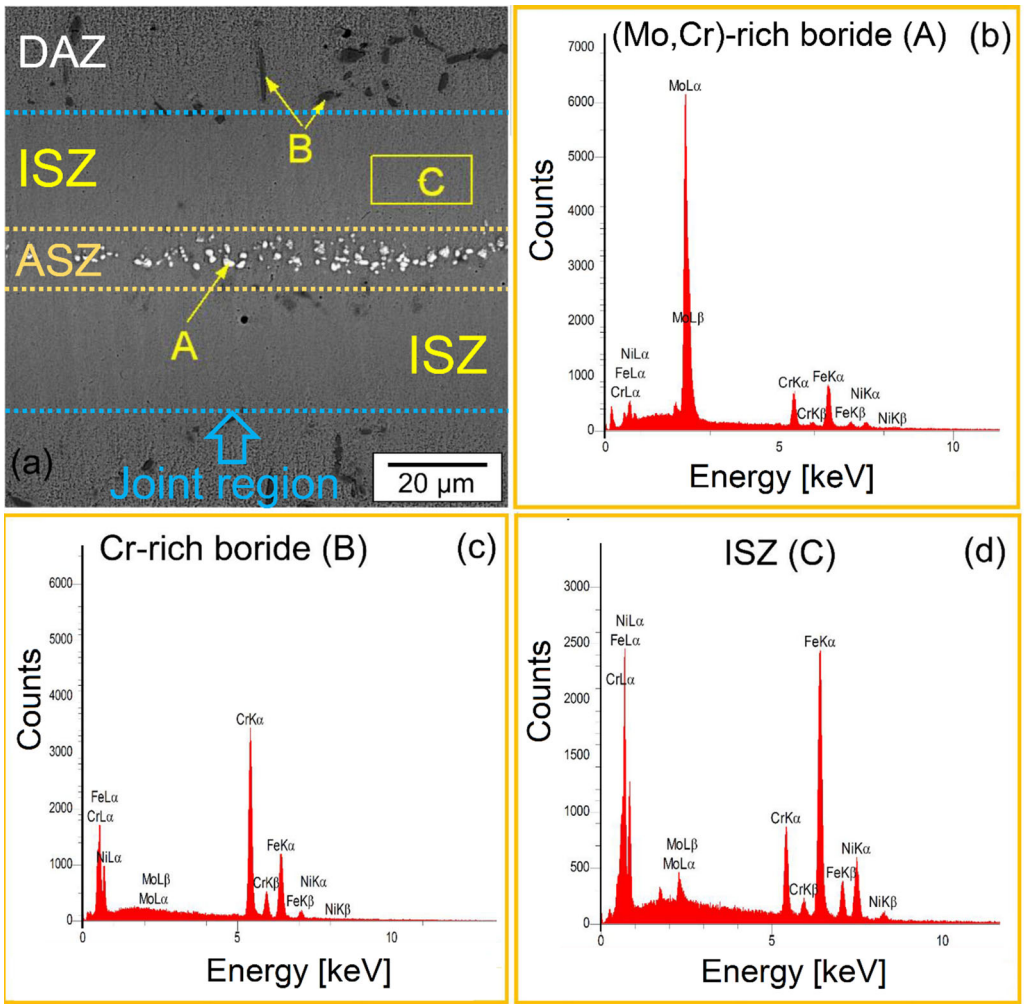

Fig. 3—(*a*) FESEM micrograph of C-TLP-bonded sample made at 1200 °C for 120 minutes (*b* through *d*) FESEM–EDS spectrum for ASZ, DAZ, and ISZ, respectively.

Table III. The Chemical Composition of Different Phases in the Joint Region of the C-TLP Bonded Sample at 1200 °C and 120 Minutes

		Element (Wt Pct)			
Zone	Microconstituent	Fe	Cr	Ni	Mo
ASZ	(Mo, Cr)-rich boride (A)*	18.1	10	2.0	69.9
DAZ	Cr-rich boride (B)*	28.6	66.5	4.2	0.7
ISZ	Fe-based solid solution (C)	62.1	15.8	15.9	6.2

*Boron and carbon could be detected by the EDS in this phase, though it could not be quantified due to the inability of the EDS system for the light elements.

solid-state diffusion of B from the solid interface toward the bulk of the AISI 304 stainless steel. This causes the deviation of the S/L interface from equilibrium conditions and diffusion of B from molten FM into the solid BM to compensate for the reduced B at the solid interface and re-establish the equilibrium conditions.[15] The depletion of B from the liquid phase into the solid phase is accompanied by the deviation of the liquid-phase concentration from the liquidus concentration to a different one in the mushy zone. Therefore, although the bonding temperature is constant, the liquid phase partially transforms into the Fe-based solid solution at the S/L interface. Thus, the single-phase austenite formed at the S/L interface is the product of a diffusion-controlled isothermal transformation. That is why this zone is known as ISZ.

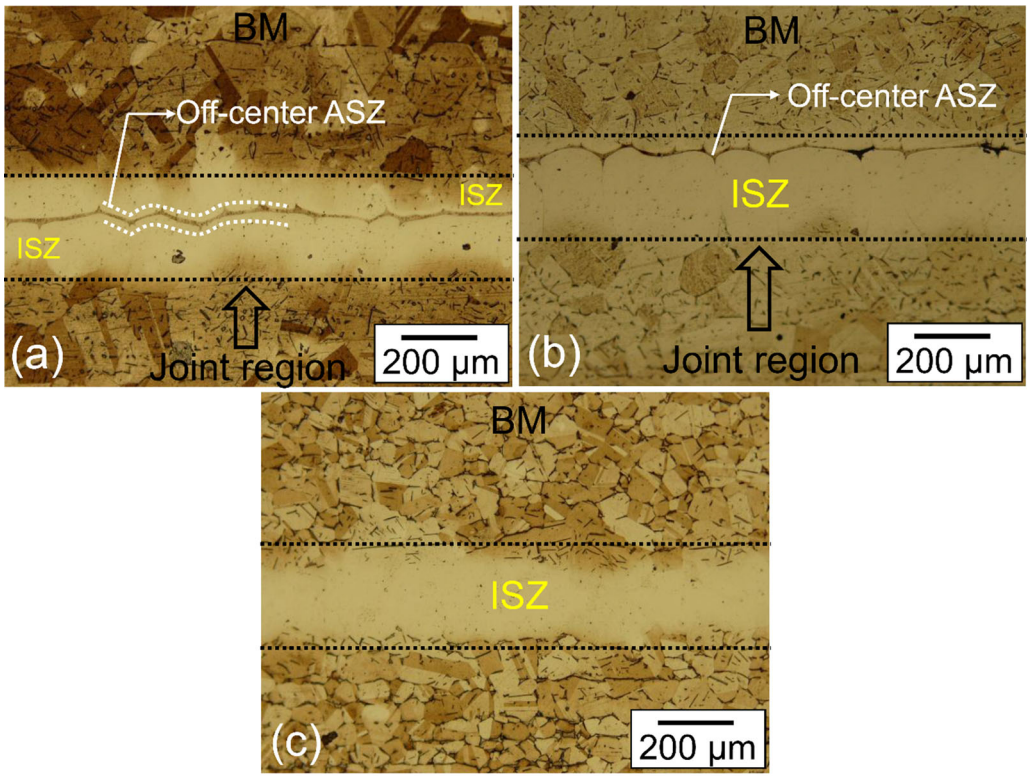

Fig. 4—Optical micrographs of TG-TLP-bonded sample made at 1200 °C for (*a*) 60 minutes, (*b*) 90 minutes, and (*c*) 120 minutes.

According to Figures 2(a) through (c), a continuous network of intermetallic constituents is in the centerline of the joint region due to the inadequate time for the depletion of B from the molten FM and the accomplishment of isothermal solidification. In other words, the remaining liquid phase at the joint region experienced an athermal solidification rather than isothermal and resulted in the formation of an ASZ at the joint region. This zone consists of a Fe-based solid solution matrix and boride micro-constituents solidified during the eutectic reaction(s). The boride precipitates in the ASZ are brittle in nature and continuous in morphology, both detrimental to the mechanical properties of the joint.[12] According to Figures 2(a) through (d), the increase in the bonding time from 45 up to 360 minutes led to the decrease in the width of the ASZ and eventually complete isothermal solidification at 1200 °C in which the ASZ is absent (Figure 2(d)).

Diffusion of B from molten FM to the AISI 304 stainless steel causes the enrichment of the BM from B atoms. When the B content of the BM exceeds the solubility limit, boride precipitation takes place. The depth of the region in which the borides are perceptible is around 110 μm in AISI 304 stainless steel (after 45 minutes holding time) and is called DAZ. The borides in the DAZ benefit from a lack of continuity, leading to lower adverse effects on the joint strength compared to the eutectic constituents formed in the ASZ.[11,12] It can be inferred from Figure 2 that the volume fraction of the precipitates in the DAZ shows a descending trend by increasing the holding time at the bonding temperature.

The SEM micrograph in Figure 3(a) shows the microstructure of the joint region at higher magnification in the sample bonded at 1200 °C for 120 minutes. The designated phases in the ASZ, DAZ, and ISZ were subjected to the EDS point analysis. The EDS spectra of the corresponding phases are provided in Figures 3(b) through (d), and the quantitative results of the chemical composition analysis are listed in Table III. According to these results, phase A in the ASZ contains the B element. The EDS results also suggest that this phase is enriched by Mo and Cr elements. Therefore, it can be concluded that the ASZ consists of a Fe-based solid solution matrix and (Mo, Cr)-rich boride phase. Based on Figure 3(c) and Table III, precipitates in the DAZ are Cr-rich borides. According to microstructure and EDS analysis of ISZ (marked as C), it can be deduced that the ISZ is a single-phase Fe-based solid solution with Cr and Ni as alloying elements, free from any precipitates. The presence of the Cr element in the joint region originates from the diffusion of the BM in the molten FM during the dissolution stage. The ASZ and/or DAZ products in other C-TLP-bonded samples were similar to the sample bonded at 1200 °C for 120 minutes.

B. *Microstructural Evolutions During TG-TLP*

The optical micrographs in Figures 4(a) through (c) illustrate the microstructural overview of the joint region in TG-TLP-bonded samples at 1200 °C for 60, 90, and 120 minutes, respectively. As opposed to the C-TLP scenario, the DAZ is not perceptible, and the

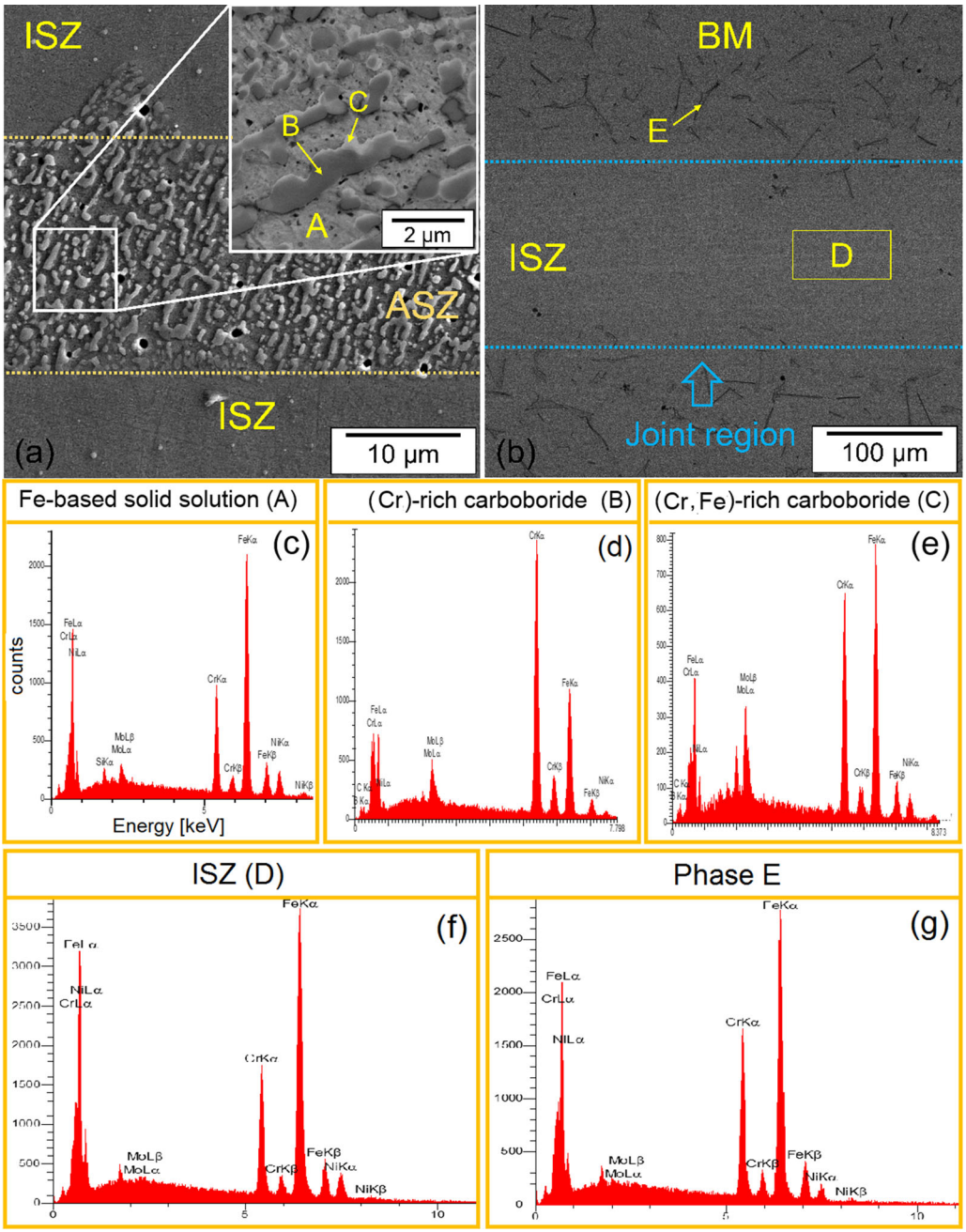

Fig. 5—FESEM micrograph of TG-TLP-bonded sample at (*a*) 1200 °C for 90 minutes and (*b*) 1200 °C for 120 minutes. The EDS spectra of the A, B, C, D, and E phases shown in the micrographs are provided in (*c* through *g*), respectively.

ASZ is not at the centerline of the joint region. Such an observation can be justified by considering the asymmetric diffusion-control solidification in the bonded samples derived from an imposed temperature gradient. According to Figure 4(c), the absence of eutectic constituents in the bonding zone confirms that the bonding time of 120 minutes is adequate for complete isothermal solidification. This is one third of the isothermal completion time of the C-TLP-bonded samples. In contrast to C-TLP, TG-TLP mainly relies on solute diffusion in the liquid phase and requires a significantly shorter isothermal solidification time.[39] The main reasons behind the shorter isothermal solidification accomplishment time in TG-TLP bonds are thoroughly scrutinized in Section IV–B.

SEM micrographs and EDS analysis results of the TG-TLP-bonded samples at 1200 °C/90 min and 1200 °C/120 min are shown in Figure 5 and Table IV, respectively. According to Figure 5(a), the ASZ in TG-TLP-bonded samples consists of three distinct phases, marked as A, B, and C. As mentioned earlier, the ASZ perceptible at room temperature is the remaining liquid phase at the bonding temperature, which could not find the chance to undergo diffusion-controlled isothermal solidification. This liquid is transformed into three phases during the cooling stage, which

Table IV. The Chemical Composition of Different Phases in the Joint Region of the TG-TLP Bonded Sample at 1200 °C for 90 and 120 Minutes

Zone	Microconstituent	Element (Wt Pct)			
		Fe	Cr	Ni	Mo
ASZ	Fe-based solid solution (A)	68.9	16.8	11.5	2.8
	Cr-rich carboboride (B)*	40	52.5	1.6	6
	(Cr, Fe)-rich carboboride (C)*	54	27.7	8.2	10.1
ISZ	Fe-based solid solution (D)	67.6	22.8	7.3	0.9
BM	Phase E	66.9	28.9	3.8	0.4

*Boron and carbon could be detected by the EDS in this phase, though it could not be quantified due to the inability of the EDS system for the light elements.

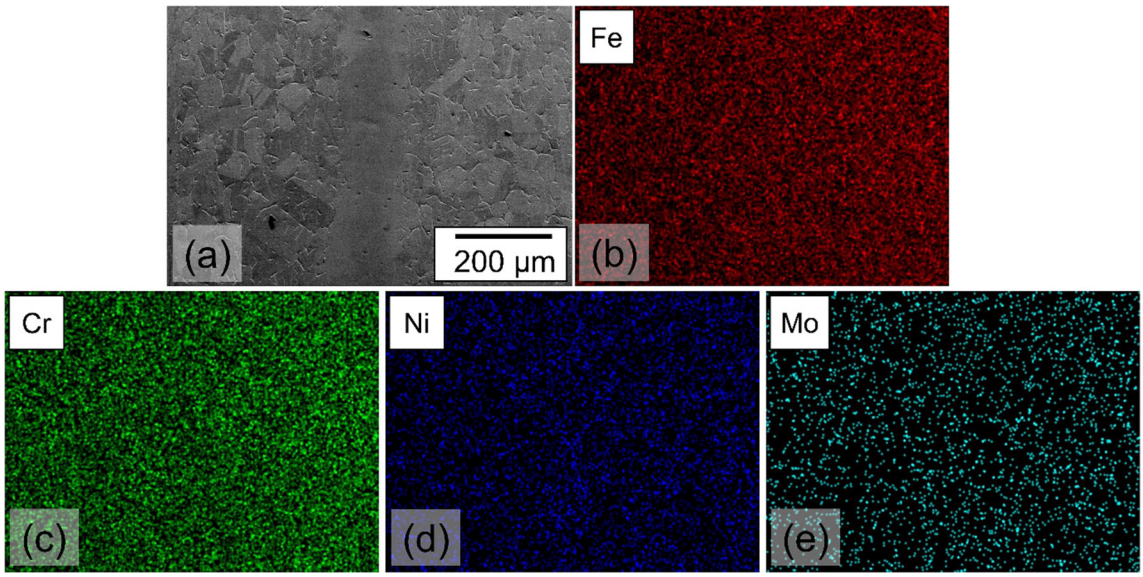

Fig. 6—The SEM micrograph of (*a*) TG-TLP-bonded sample after completion of the isothermal solidification. The EDS chemical composition maps showing the elemental distribution in this micrograph of Fe, Cr, Ni, and Mo are provided in (*b* through *e*).

are Fe-based solid solution matrix enriched by Ni and Cr (A), Cr-rich boride (B), and (Cr, Fe)-rich boride (C), as suggested by the chemical compositions provided in Table IV. The single phase shown in Figure 5(b), marked as phase D, formed at the bonding temperature after the accomplishment of the isothermal solidification. Comparing the quantity of Mo of ASZ constituents to that of the Fe-based solid solution in the ISZ, the former has noticeably higher Mo content. Another phase-labeled E was observed in the BM of the TG-TLP-bonded sample, which has almost the same chemical composition as the austenite grain. However, its Cr and Ni concentrations are higher and lower than those of the BM, respectively. The phases detected in ASZ, DAZ, and/or BM of other TG-TLP-bonded samples were similar to the sample bonded at 1200 °C for 90 minutes.

Figure 6 shows the elemental distribution maps of Fe, Cr, Ni, and Mo in the TG-TLP-bonded sample after the accomplishment of the isothermal solidification. Although the TLP-bonded samples usually require a homogenization heat treatment after the isothermal solidification,[14] it is not required for the TG-TLP-bonded sample since the alloying elements detected in the ISZ are comparable to those of the BM.

C. *Influence of Bonding Cycles on the BM*

In the TLP bonding process, the whole BM/FM/BM system experiences the bonding thermal cycle. Thus, the region defined as the BM in the TLP-bonded samples is actually a heat-affected zone (HAZ) since it has experienced the bonding temperature during the process. On this account, a microstructure different from the as-received state may be obtained for the BM after experiencing the bonding thermal cycle. Therefore, investigating the BM after the TLP bonding process is crucial to understanding whether the bonding thermal cycle had detrimental effects on the BM. Figure 7 shows the microstructure of the BM in the as-received condition and after performing C-TLP and TG-TLP processes. As shown in Figure 7(a), the as-received BM contains equiaxed austenite grains with a mean size of 24 μm. The size of the gains increased remarkably after the C-TLP bonding process, especially for prolonged bonding times of 240 and 360 minutes (Figure 7(b)), in

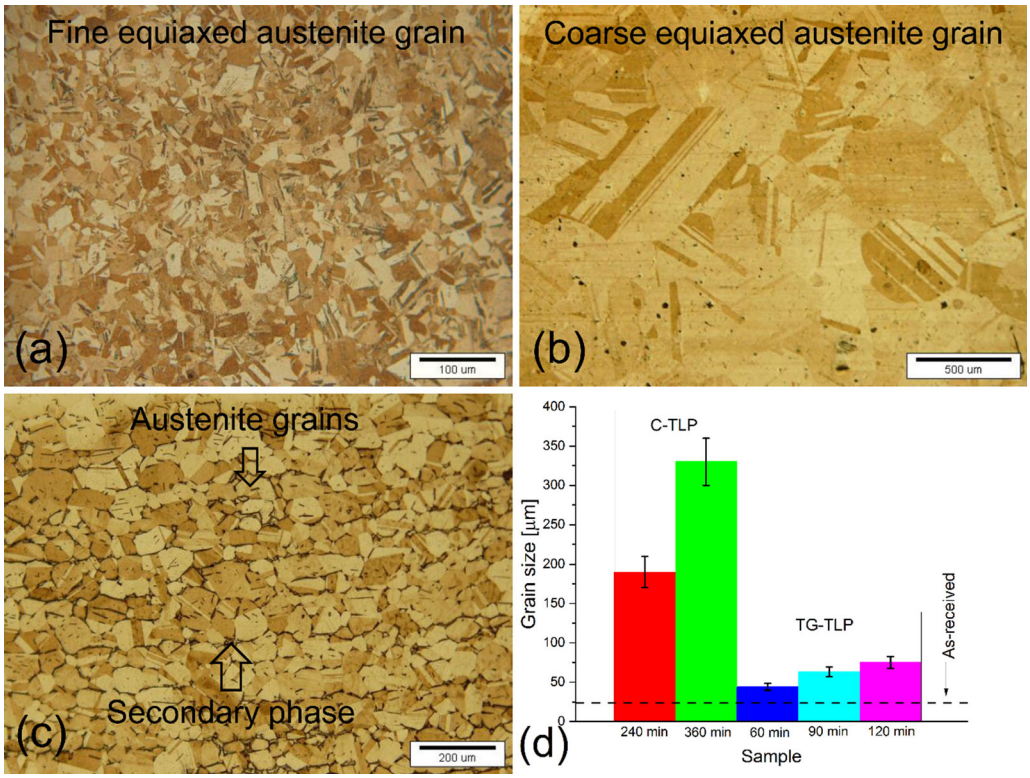

Fig. 7—Optical micrographs of BM (*a*) in the as-received condition, (*b*) after C-TLP bonding at 1200 °C/360 min, and (*c*) after TG-TLP bonding for 120 minutes. The grain size quantitative measurement results of the as-received BM, as well as the C-TLP and TG-TLP-bonded BM, are shown in (*d*).

which the mean grain size increased to 190 and 330 μm, respectively. The driving force behind the observed grain growth, which happens at temperatures higher than 1040 °C in AISI 304 stainless steel,[45] is the reduction of the grain boundary surface area through the growth of the larger grains at the expense of the smaller ones.[46] The grain growth was limited in the case of TG-TLP bonding since the holding time was significantly shorter than the C-TLP bonding process. When the isothermal solidification is accomplished, the mean grain size of the BM in the TG-TLP-bonded sample is 75 μm. Despite being noticeably larger than the as-received BM, the grains are considerably smaller than those of the BM of the C-TLP-bonded sample. Another important observation is the formation of a secondary phase in the BM after the TG-TLP bonding process. As the EDS spectrum in Figure 5(g) and the quantitative chemical composition results in Table IV suggest, the concentration of Cr (as a ferrite stabilizer) is ~ 60 pct higher than that of the austenite grains (Table I). The nature of this phase and the mechanism behind its formation are thoroughly scrutinized in Section IV–D.

D. *Mechanical Properties*

Mechanical properties were studied on the optimum samples in terms of isothermal solidification time. Since the TG-TLP bonding process benefits from significantly reduced isothermal solidification time, making it more interesting for industrial applications, C-TLP-bonded samples were excluded from microhardness and shear strength measurements. The microhardness profile across the joint region of the TG-TLP-bonded samples with bonding times of 90 and 120 minutes (before and after accomplishment of isothermal solidification) is shown in Figure 8. In Figure 8(a), the minimum and maximum hardness values are for the ISZ and ASZ, respectively. While the former is attributable to the higher concentration of Ni and lower concentration of Cr than the BM in the ISZ, the latter originates from brittle and hard eutectic compounds in the ASZ. According to Figure 8(b), the hardness of the ISZ and BM has increased by increasing bonding time, and the difference between the microhardness values has decreased.

The shear test was conducted on the TG-TLP-bonded sample at 1200 °C/120 min (complete isothermal solidification). The heat-treated AISI 304 stainless steel (BM-HT) was subjected to the same thermal cycle. The engineering stress–strain curves are shown in Figure 8(c), and the ultimate shear strengths are shown in Figure 8(d). As it is evident, the shear strength of the TG-TLP-bonded sample is almost equal to that of the BM-HT. Therefore, the produced joint by the TG-TLP bonding process can be considered an ideal joint with ~ 100 pct efficiency from the room-temperature shear strength perspective. Figure 9 reveals the cross section of the fractured surface after the shear test. As shown in Figure 9(a), the crack grew in the BM, meaning that this region behaved as the weakest

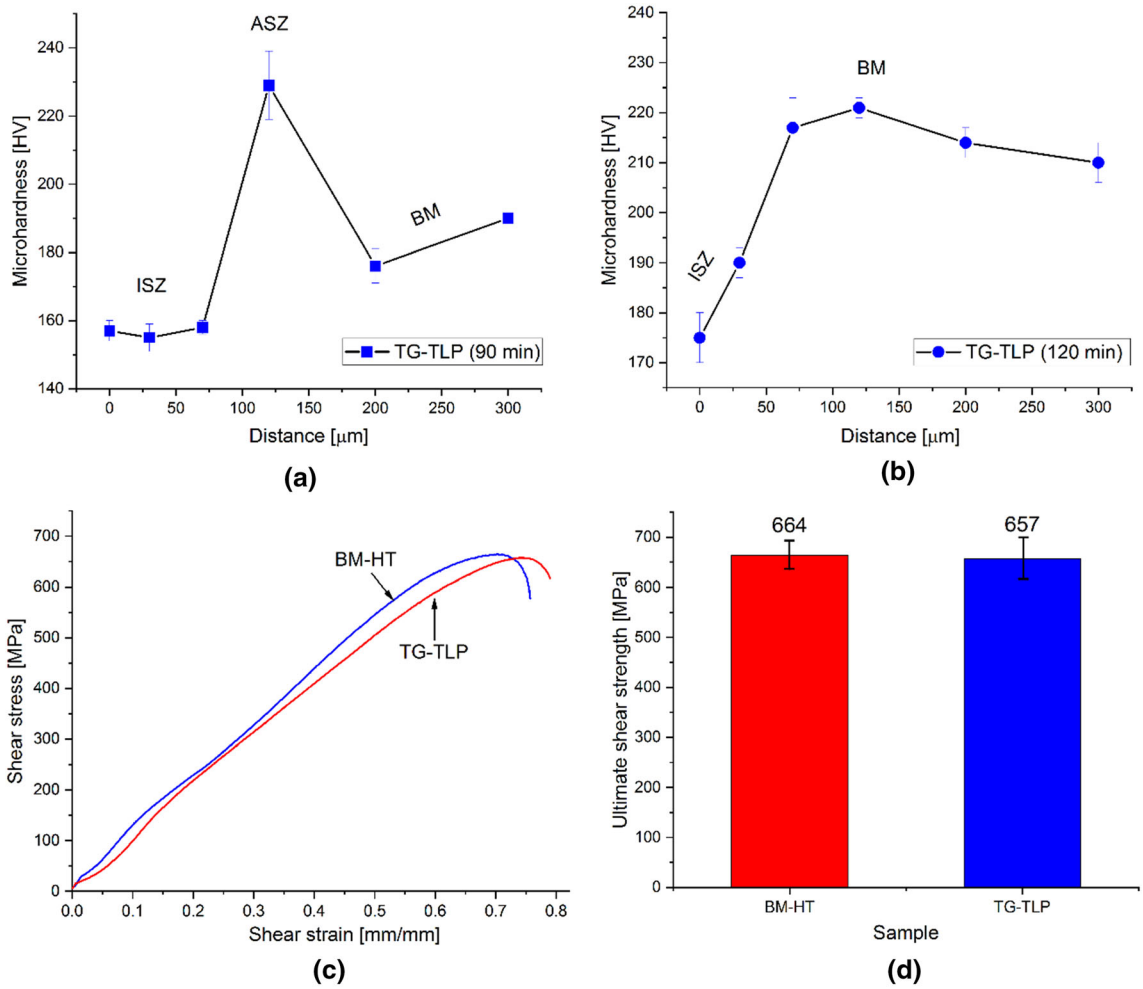

Fig. 8—Microhardness profile across the joint region in the TG-TLP-bonded samples at 1200 °C for (*a*) 90 minutes, (*b*) 120 minutes, (*c*) shear stress–strain curves for TG-TLP-bonded sample at 1200 °C and heat-treated AISI 304 stainless steel (BM-HT), and (*d*) the ultimate shear strength of the TG-TLP-bonded sample at 1200 °C and heat-treated AISI 304 stainless steel (BM-HT).

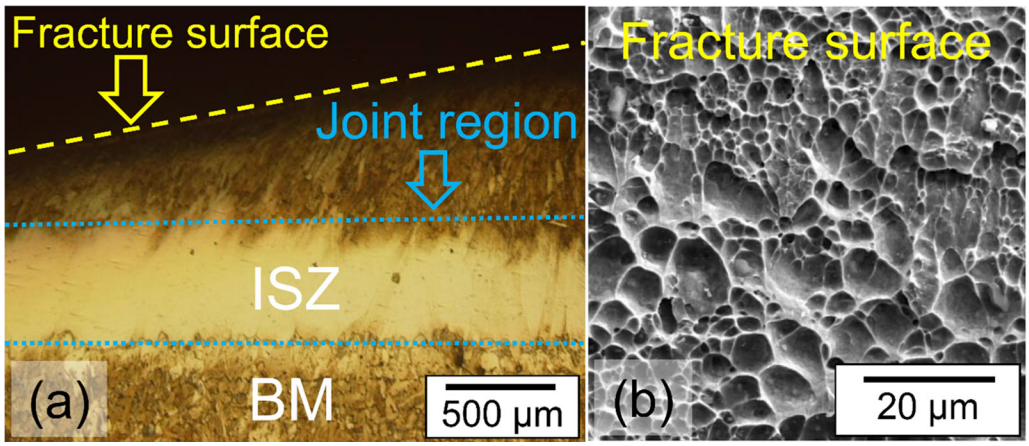

Fig. 9—Optical micrograph of failure path (*a*) starting of propagation crack and (*b*) continues growing crack.

position of this bond; consequently, the crack propagation and failure took place in the BM. Figure 9(b) shows the SEM micrograph of the fracture surface in which fine and coarse dimples are perceptible, confirming the ductile fracture of the specimen during the shear test.

Table V. Chemical Composition of the Joint Region in the C-TLP and TG-TLP Bonded Samples at the Maximum Gap Width

	C-TLP			TG-TLP		
Element	From BM (g)	From FM (g)	Total (Wt Pct)	From BM (g)	From FM (g)	Total (Wt Pct)
Fe	0.0292	0.0204	57.7	0.2588	0.0204	70.0
Ni	0.00328	0.0204	27.6	0.0291	0.0204	12.4
Cr	0.00731	0	8.5	0.0647	0	16.2
Mo	0	0.00351	4.1	0	0.00351	0.88
C	5.176×10^{-6}	0	0.006	4.584×10^{-5}	0	0.011
B	0	0.00178	2.07	0	0.00178	0.446

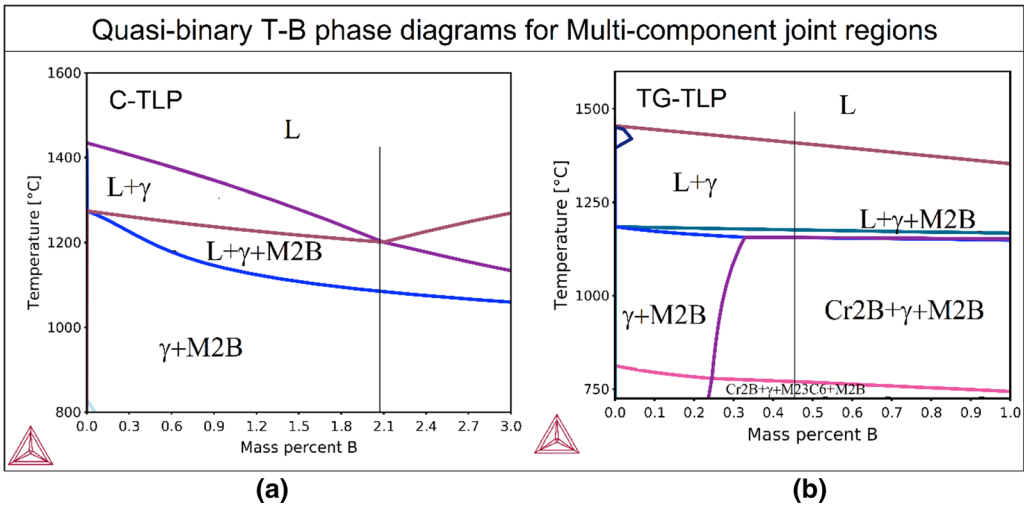

Fig. 10—Equilibrium T–B isopleths for (*a*) C-TLP and (*b*) TG-TLP systems. The vertical line in both diagrams shows the chemical compositions provided in Table V.

IV. DISCUSSION

A. *Solidification Path-C-TLP vs. TG-TLP*

The SEM micrograph in Figure 3(a) shows the microstructure of the joint region at high magnification in the sample bonded at 1200 °C for 120 minutes. The designated phases in the ASZ, DAZ, and ISZ were subjected to the EDS point analysis. The EDS spectra of the corresponding phases are provided in Figures 3(b) through (d), and the quantitative results of the chemical composition analysis are listed in Table III. According to these results, phase A in the ASZ is a boride with a significant amount of Mo and Cr elements. Therefore, it can be concluded that the ASZ consists of a Fe-based solid solution matrix and (Mo, Cr)-rich boride phase. Based on Figure 3(c) and Table III, precipitates in the DAZ are Cr-rich borides. According to microstructure and EDS analysis of ISZ (marked as C), it can be deduced that the ISZ is a single-phase Fe-based solid solution with Cr and Ni as alloying elements, free from any precipitates. The presence of the Cr element in the joint region originates from the diffusion of the BM in the molten FM during the dissolution stage. According to Figure 3 and Table III for C-TLP-bonded sample, as well as Figure 5 and Table IV for the TG-TLP-bonded sample, it can be inferred that these two bonding strategies led to the formation of different solidification products in the ASZ when the isothermal solidification is not completed. Studying the solidification path in the ASZ is highly important, especially in cases with prolonged isothermal solidification time, such as repairing wide-gap cracks in turbine blades after several hours of operation.[12] Since being cost prohibitive, the TLP bonding process is usually substituted by short brazing cycles in such circumstances in which the formation of ASZ is unavoidable. Finding the solidification path helps[11] (i) understand the maximum service temperature and (ii) design suitable heat treatment cycles for the brazements based on the formation temperature of the final solidification products. Moreover, depending on the nature of borides formed in the ASZ, the mechanical response of the joint can be predicted.

To embrace the discussion of solidification products in the ASZ, the calculation of the liquid-phase chemical composition after the dissolution of the BM (at maximum gap size) was exercised. According to Figures 2(b) and 4(b), the width of the joint region is 75 and 350 μm after 120 and 90 minutes holding time at the bonding temperature for C-TLP and TG-TLP-bonded samples, respectively. Given that the gap size was fixed at 40 μm (thickness of the Fe–Ni–Mo–B FM) for both samples before bonding, it is fair to conclude that the increase in the width of the joint region happened due to the dissolution of the BM during the process. The mass of

BM participated in the joint region (M_{BM}^{Joint}) can be calculated using the following equation:

$$M_{BM}^{Joint} = A(W_{max} - W_0)\rho_{BM}, \quad [3]$$

in which A, W_0, W_{max}, and ρ_{BM} denote the surface area of TLP bonding specimens (1.44 cm^2), FM width, maximum gap width, and density of the AISI 304 stainless steel (7.9 g/cm^3), respectively. The M_{BM}^{Joint} was found to be 0.03982 and 0.35266 g for C-TLP and TG-TLP samples, respectively. The mass of the FM in the joint region (M_{FM}^{Joint}) can be calculated using the following equation:

$$M_{FM}^{Joint} = AW_0\rho_{FM}, \quad [4]$$

where ρ_{FM} is the density of the liquid FM at the bonding temperature (8 g/cm^3). The ρ_{FM} was calculated using the chemical composition of FM using the JMatPro Software, NiFe-based superalloy database. The M_{FM}^{Joint} was found to be 0.04608 g. By utilizing the above equations along with the chemical compositions of the BM and FM provided in Table I, the chemical composition of the joint region after the dissolution was determined (Table V).

To predict the solidification sequence of the ASZ, multi-component isopleths were calculated for the C-TLP and TG-TLP joint regions using Thermo-Calc Software, TCFE6: Steels/Fe-Alloys database version 6.2. The solidification path explained has two simplified assumptions: (i) the composition of liquid does not vary with time, and (ii) no diffusion can happen after the solidification of FM till the end of the isothermal hold. A more accurate solidification path can be obtained by an isothermal Dictra simulation and is not in the scope of this study. The calculated T–B isopleths are shown in Figure 10. In both diagrams, the left-hand endmember is fixed at the B-excluded chemical composition of the joint regions, and the X-axis shows the mass percent B. Since Fe is defined as the dependent element in the calculations, only Fe is substituted by the B element in these isopleths. The vertical lines in Figures 10(a) and (b) are at 2.07 and 0.446 wt pct B, where the chemical composition is equal to Table V for C-TLP and TG-TLP cases, respectively.

According to Figure 10(a), the predicted solidification path for the C-TLP joint region is as follows:

$$L \rightarrow L + \gamma_{Fe} + M_2B \rightarrow \gamma_{Fe} + M_2B \quad [5]$$

in which γ_{Fe} is the austenite and M_2B is $(Mo, Cr, Fe, Ni)_2B$ boride which is Mo and Cr rich. Table III proves that these phases are Fe-based solid solution (matrix) and (Mo, Cr)-rich boride. Thus, the predicted solidification path by Thermo-Calc Software is completely in line with the microstructural observations and EDS chemical composition analysis of the ASZ in the C-TLP-bonded sample, and it is fair to conclude that the matrix is γ_{Fe} and the detected boride is M_2B phase.

According to Figure 10(b), the predicted solidification path for the TG-TLP joint region is as follows:

$$L \rightarrow L + \gamma_{Fe} \rightarrow L + \gamma_{Fe} + M_2B \rightarrow \gamma_{Fe} + M_2B + Cr_2B, \quad [6]$$

in which M_2B is $(Cr, Mo, Fe, Ni)_2B$ boride, which is (Cr, Mo) rich and Cr_2B is actually $(Cr, Fe)_2B$ boride. Referring to Figure 10(b), a solid-state transformation was also observed in the TG-TLP system:

$$\gamma_{Fe} + M_2B + Cr_2B \rightarrow \gamma_{Fe} + M_2B + Cr_2B + M_{23}C_6, \quad [7]$$

in which $M_{23}C_6$ is defined as $(Cr, Fe, Mo)_{23}(C, B)_6$. Based on the microstructural investigations as well as the EDS analysis results provided in Figure 5(a) and Table IV, Fe-based solid solution (matrix), Cr-rich, and (Cr, Fe)-rich borides/carboborides were detected in the ASZ of the TG-TLP-bonded sample, meaning that the respective phases are γ_{Fe}, Cr_2B, and $M_{23}C_6$. The M_2B phase was absent in the ASZ of the TG-TLP-bonded sample, despite predicted in the Thermo-Calc calculations. As it is evident in Figure 10(b), the formation of M_2B phase occurs in a narrow temperature range (1170 °C to 1150 °C) at equilibrium conditions. It means that minor changes in the chemical composition might result in the disappearance of this phase transformation in the quasi-binary phase diagrams. Given the fact that the chemical compositions (Table V) used to predict the solidification path by Thermo-Calc Software were only an estimation based on the dissolution width ($W_{max} - W_0$) of the BM and the nominal chemical composition of the FM, such discrepancies are justifiable. Moreover, it is highly probable that due to the rapid solidification associated with the air cooling of the TG-TLP-bonded sample, equilibrium conditions have not been satisfied during the athermal solidification, which hinders the formation of this phase. Therefore, the real solidification path along with the solid-state transformations in the TG-TLP-bonded sample is as follows:

$$L \rightarrow L + \gamma_{Fe} \rightarrow \gamma_{Fe} + Cr_2B \rightarrow \gamma_{Fe} + Cr_2B + M_{23}C_6. \quad [8]$$

Based on the abovementioned discussion and the explored solidification paths, it can be concluded that the microstructure of the ASZ is controlled by the formation of primary γ_{Fe} and partitioning of the B and/or C as elements with negligible solubility in this phase in both TLP bonding conditions. In C-TLP, the dissolution of the BM is significantly lower than that of the TG-TLP, meaning that the chemical composition of the liquid phase at the maximum gap width is closer to the starting FM than BM. In other words, the concentration of Mo, as an element with a higher affinity than Cr to react with B, was still high enough to result in the formation of (Mo, Cr)-rich borides in the ASZ. In the TG-TLP bonding, on the other hand, the Cr and C concentration was significantly higher than the

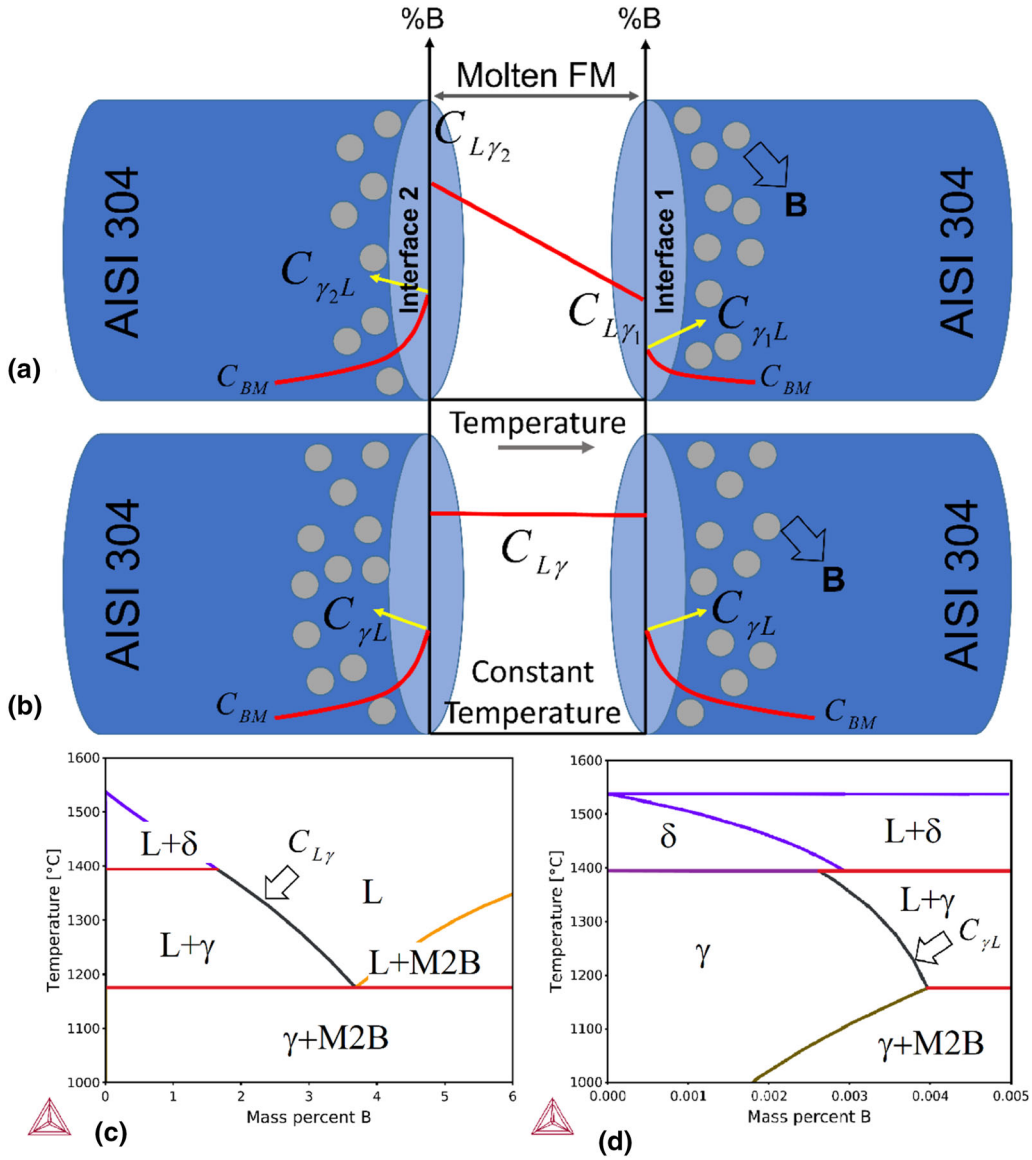

Fig. 11—Schematic illustration of (*a*) TG-TLP and (*b*) C-TLP-bonded samples in tandem with the concentration profile across the joint region and within the BMs. The equilibrium Fe–B binary phase diagram in two different mass pct B ranges is shown in (*c*) and (*d*), proving that the $C_{L\gamma}$ and $C_{\gamma L}$ decrease with increasing the temperature.

C-TLP case due to its noticeably higher dissolution rate of BM (310 μm in TG-TLP compared to 35 μm in C-TLP). This led to the change in the solidification path and formation of Cr-rich and (Cr, Fe)-rich borides/carboborides in the ASZ of the TG-TLP-bonded sample. It is believed that the $M_{23}C_6$ phase could find the chance to form through a solid-state transformation.

Based on Figure 2(a) for C-TLP bonding at 1200 °C/45 min and Figure 4(a) for TG-TLP bonding at 1200 °C/60 min, it can be understood that the ASZ width is very narrow (7.7 μm for C-TLP *vs.* 9 μm for TG-TLP bonding). Besides, γ_{Fe} phase with high toughness exists between hard and brittle borides and carboborides. Therefore, depending on the requirements of the application, the brazements in which the isothermal solidification is not accomplished can also be used. It is worth noting that the TG-TLP bonding process enables higher service temperature since the final solidification product was formed at 1150 instead of 1080 °C for C-TLP bonding.

B. *Isothermal Solidification Time*

Referring to Figures 2 and 4, it is self-evident that the isothermal solidification was accomplished at a noticeably shorter time of 120 minutes in the TG-TLP compared to the 360 minutes in the C-TLP bonding process. This phenomenon can be explained by the asymmetric diffusion-controlled solidification derived from an imposed temperature gradient in the TG-TLP-bonded sample. Figure 11 schematically illustrates the B concentration profile across the joint region

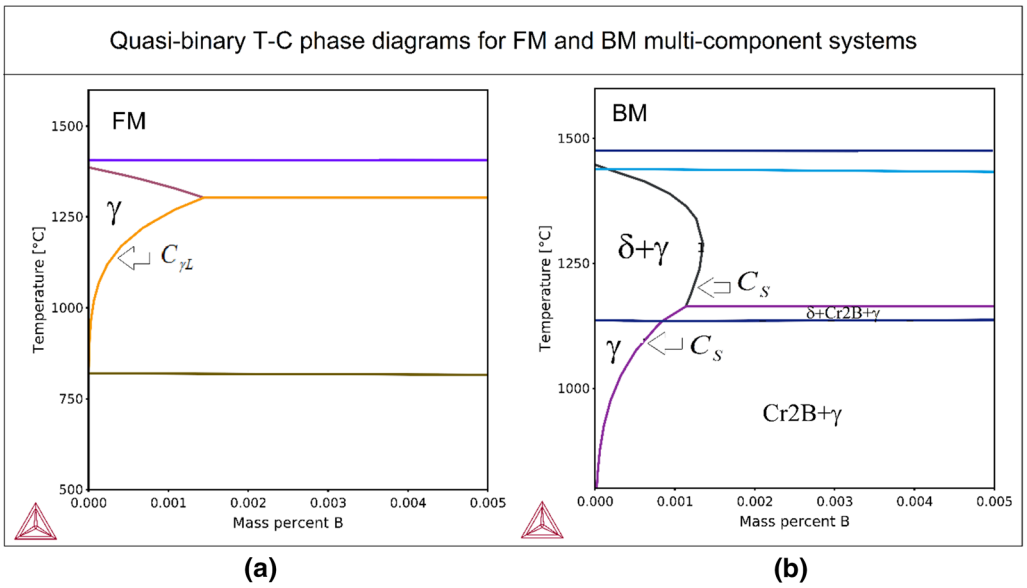

Fig. 12—The equilibrium (*a*) B-excluded FM *vs.* B, and (*b*) BM *vs.* B isopleths.

and within the BM in the TG-TLP and C-TLP-bonded samples. In the C-TLP bonding of the AISI 304 stainless steel, the TLP system is symmetrical since the whole system is at a constant bonding temperature. The equilibrium concentration of B in the solid and liquid phases in this system is named as $C_{\gamma L}$ and $C_{L\gamma}$, respectively (Figure 11(b)). In this case, there is merely a B concentration gradient in the solid phase, not in the liquid phase. Therefore, it can be deduced that the isothermal solidification in the C-TLP bonding process is only controlled by the solid-state diffusion of B within the BM due to the presence of a B concentration gradient between the solid interface and the bulk of the BM ($C_{\gamma L} - C_{\mathrm{BM}}$).[15]

In the case of temperature gradient (TG-TLP bonding in Figure 11(a)), on the other hand, two S/L interfaces exist in the TLP bonding system with different temperatures. In the schematic illustration in Figure 11(a), it is assumed that interface (1) is at a higher temperature than interface (2). The equilibrium B concentrations in the solid and liquid phases are named as $C_{\gamma_1 L}$ and $C_{L\gamma_1}$ for interface (1) and $C_{\gamma_2 L}$ and $C_{L\gamma_2}$ for interface (2). It is evident from the equilibrium Fe–B binary phase diagrams shown in Figures 11(c) and (d) that the increase in temperature decreases the $C_{\gamma L}$ and $C_{L\gamma}$ values. This unravels the reason behind the lower $C_{\gamma_1 L}$ and $C_{L\gamma_1}$ at the interface (1) (Figure 11(a)) compared to their corresponding values at the interface (2). Therefore, in addition to the solid-state B concentration gradient within the BM, a liquid-state concentration gradient exists in the liquid phase, which plays a crucial role in the isothermal solidification.[39] At interface (2), B atoms diffuse in two different directions:(i) outflux from the interface into the BM and (ii) outflux from the interface into the liquid phase toward interface (1), both encouraging the isothermal solidification through solid-state and liquid-state diffusion processes, respectively.[40] In other words, both of these outflux diffusions reduce $C_{L\gamma_2}$ and cause the liquid phase to enter the mushy zone (Figure 11(c)), which results in the progression of the interface (2) toward the joint centerline. At interface (1), on the other hand, B outflux from the interface into the bulk of the BM and the B influx from the liquid phase take place.[40] Although the solid-state diffusion of B into the BM results in the isothermal solidification, the liquid-state diffusion due to the concentration gradient in the liquid phase increases the $C_{\gamma_1 L}$ (Figure 11(d)), which causes the melting of the interface (1). At the beginning of the isothermal solidification, when the concentration of B is zero in the BM, the isothermal solidification overcomes the melting of the interface (1).[40] This can be seen in Figure 4(a) for the TG-TLP-bonded sample after 60 minutes, in which the isothermal solidification has occurred from both interfaces. Bypassing time and reducing the concentration gradient of B in the BM, the liquid-state diffusion prevails. Consequently, interface (1) experiences melting, which results in the migration of this S/L interface toward the BM. At this stage, solidification occurs only at the low-temperature interface [interface (2)], and the temperature gradient produces asymmetric diffusional solidification. The overview of the joint region in the TG-TLP-bonded samples shown in Figure 4(b) gives evidence of such a unidirectional migration of one of the S/L interfaces during the TG-TLP bonding process. As can be seen, the ASZ is off-center and close to one of the BMs in this case rather than at the joint centerline similar to the C-TLP-bonded sample (Figure 2).

Based on the above discussion, the isothermal solidification should be faster in the TG-TLP than the C-TLP bonding process due to the liquid-state isothermal solidification control of the cooler S/L interface. Since the diffusion flux of B in the liquid is at least an order of magnitude greater than solid,[47] the isothermal solidification time in the case of TG-TLP bonding was expected to be 10 times shorter than the C-TLP bonding

process at the minimum. However, the larger width of the joint region in the TG-TLP-bonded sample than in the C-TLP-bonded one (350 *vs.* 75 μm), along with the unidirectional solidification in the presence of the temperature gradient, can compensate for the influence of liquid-state diffusion on the isothermal solidification. Nevertheless, there is still a great difference between the isothermal solidification time of the TG-TLP-bonded and C-TLP-bonded samples (120 *vs.* 360 minutes), making the former cost and time effective for industrial applications.

It is worth noting that as long as the excessive dissolution of the BM does not result in the prolonged isothermal solidification time, it is believed to be beneficial since it increases the amount of BM-alloying elements in the joint region. For instance, in the TG-TLP-bonded AISI 304 stainless steel, higher Cr content was detected in the ISZ than in the C-TLP-bonded sample, which improves the corrosion resistance of the joint and enhances its mechanical properties. Referring to Figure 6, a uniform distribution of the Cr, Ni, and Mo was detected in the TG-TLP-bonded sample (120 minutes) by the EDS elemental maps, confirming the formation of a joint region with a chemical composition almost equal to that of the BM. This is also in line with the quantitative chemical composition analysis results of the ISZ of the TG-TLP-bonded sample after completion of isothermal solidification (Table IV). However, the Cr concentration of the ISZ in the C-TLP-bonded sample is significantly lower than that of the BM due to the lower dissolution.

C. *Diffusion Affected Zone*

Referring to the optical micrographs in Figures 2 and 4, boride precipitates are perceptible in the DAZ of the C-TLP-bonded samples. However, they are absent in the TG-TLP-bonded ones. To justify such an observation, the mechanism behind the formation of borides in the DAZ during the TLP bonding process needs to be explored. As explained in Section IV–B, an equilibrium B concentration can be defined for the solid phase at the S/L interface, $C_{\gamma L}$, which its value is greater than the B concentration at any point within the BM (Figures 11(a) and (b)). Based on Figure 12(a) for the binary Fe–B phase diagram, $C_{\gamma L}$ is basically the maximum solubility limit of the B in the solid phase at the interface. For the AISI 304/FM/AISI 304 multi-component system, the $C_{\gamma L}$ may be different from that of the Fe–B binary case. Assuming that the first layer of the solidified liquid phase at the solid BM has a chemical composition equal to that of the B-excluded FM, the $C_{\gamma L}$ can be estimated from the FM equilibrium isopleth (Figure 12(a)). Since the chemical composition of the solid phase at the S/L interface is different from that of the BM, an equilibrium B concentration can also be defined for the bulk of the BM (C_S) using the BM equilibrium isopleth (Figure 12(b)). The C_S is basically the maximum solubility limit of the B in the bulk of the BM. In the diagrams shown in Figure 12, the left-hand endmember is the B-excluded FM (Figure 12(a)) or BM (Figure 12(b)) chemical composition, and the *X*-axis is the mass percent B. Boride formation in the DAZ during the depletion of B from the liquid phase, and diffusion into the solid phase in the isothermal solidification stage occurs if and only if the C_S of the BM is lower than the $C_{\gamma L}$ of the FM. As shown in Figure 12, the C_S for AISI 304 stainless steel is greater than $C_{\gamma L}$ at the bonding temperature. Given the fact that the B concentration in the bulk of the AISI 304 stainless steel is always lower than that of the solid phase at the S/L interface (Figures 11(a) and (b)), and $C_S > C_{\gamma L}$ in the AISI 304/Fe–Ni–Mo–B/AISI 304 system, the boride precipitation should not happen during the isothermal solidification.

Although no DAZ was found in the TG-TLP-bonded samples (Figure 4), boride formation in the DAZ of the C-TLP-bonded samples was confirmed by optical and SEM micrographs shown in Figures 2 and 3(a). The DAZ formation in the C-TLP bonding case seems to contradict the Thermo-Calc calculation results at first glance. To resolve this contradiction, it should be noted that the boride formation can still happen in the melting and dissolution stages of the TLP bonding process[48] before the equilibrium conditions are established at the S/L interface. On this account, borides can form in the DAZ from the solidus temperature (T_S) of the FM (~ 1000 °C) up to the bonding temperature (before the isothermal solidification is started). In the case of C-TLP bonding with the heating rate of 40 °C/min, the total time before establishing equilibrium conditions is ~ 5 minutes, which is more than enough for boride formation in the DAZ. In the TG-TLP bonding process, on the other hand, the temperature reaches the bonding temperature in a few seconds, explaining the absence of borides in these samples. It is worth noting that the formation of borides in the DAZ consumes the boron atoms and creates boron-free regions around the borides providing a steep gradient for B diffusion in the BM.[49] Therefore, if the C-TLP bonding was performed in the induction furnace, the isothermal solidification time would be longer than in the box furnace. In other words, the difference between the isothermal solidification completion times of the C-TLP-bonded and TG-TLP-bonded samples cannot be merely attributed to the imposed temperature gradient in the latter but to the boride formation in the DAZ of the former.

To understand whether the DAZ formation in the C-TLP-bonded samples is attributable to the melting and dissolution stages, the B diffusion distance in the temperature range of 1000 °C to 1200 °C (1273 K to 1473 K) with the heating rate of 40 °C/min was calculated and compared to the width of the DAZ in the optical micrograph shown in Figure 2(a). The diffusivity of B in γ_{Fe} ($D_B^{\gamma_{Fe}}$) can be calculated using the following equation[50]:

$$D_B^{\gamma_{Fe}}\ (\mathrm{cm}^2/\mathrm{s}) = 2 \times 10^{-3} \exp\left(\frac{-21,000\ \mathrm{cal}}{RT}\right), \quad [9]$$

where R is the gas constant and T is the absolute temperature. An equilibrium diffusivity can be defined for

the mentioned temperature range using the following equation:

$$D_{\mathrm{eq,B}}^{\gamma_{\mathrm{Fe}}} = \frac{\int_{T_S}^{T_{\mathrm{Bonding}}} D_{\mathrm{B}}^{\gamma_{\mathrm{Fe}}} \mathrm{d}T}{\Delta T} = \frac{\int_{T_S}^{T_{\mathrm{Bonding}}} 2 \times 10^{-3} \exp\left(\frac{-21{,}000}{RT}\right) \mathrm{d}T}{T_{\mathrm{Bonding}} - T_S}. \quad [10]$$

The B diffusion distance (d_B) can be approximately calculated using Eq. [11]:

$$d_B = \sqrt{D_{\mathrm{eq,B}}^{\gamma_{\mathrm{Fe}}} \Delta t}, \quad [11]$$

in which Δt is the time during which boride precipitation takes place (~ 5 minutes for C-TLP bonding). Using the above equations, the d_B would be 170 μm. Given that the width of the DAZ (110 μm) in the C-TLP-bonded sample at 1200 °C/45 min is lower than the calculated values, it can be concluded that the boride precipitation happens during the melting and dissolution stages of the TLP bonding process. The reason behind the absence of DAZ in the TG-TLP-bonded samples is the rapid heating in the 1000 °C to 1200 °C range. It is worth noting that the calculated d_B is the nominal DAZ width before the start of the isothermal solidification stage. The width of the DAZ decreases as time passes since the borides find the chance to dissolve in the matrix. This was confirmed by the optical micrographs provided in Figure 2. This can be one of the sources of the discrepancy observed between the calculated d_B and the measured DAZ width. Moreover, the diffusion data for B diffusion in pure Fe were used for the AISI 304 stainless steel in these calculations, which can also be another reason behind the difference between the calculated and experimental values.

According to Table III, the boride precipitates in the DAZ of the C-TLP-bonded samples are Cr-rich borides. According to Figure 12(b), these are Cr_2B borides ($(Cr, Fe)_2B$ based on Thermo-Calc definition of this phase) that form between 1000 °C and 1161 °C in the AISI 304 stainless steel. Although such discontinuous borides in the DAZ are proved to have negligible influence on the mechanical properties, they might be significantly detrimental to the corrosion resistance of the joint. This is because the formation of Cr_2B borides is inevitably accompanied by the creation of Cr-free regions, prone to local oxidation. Therefore, not only from the isothermal solidification completion time but also from the DAZ viewpoint, the TG-TLP bonding process is believed to be a better joining technique.

D. *Influence of Bonding Cycle on the BM*

According to Figures 7(a) and (b), the fine austenite grains of the as-received AISI 304 stainless steel coarsened significantly during the C-TLP bonding process. For instance, after completion of the isothermal solidification (360 minutes), the mean grain size of the BM was found to be about 13 times greater than the as-received condition (Figure 7(d)). Based on the previous studies on the grain-coarsening behavior of AISI 304 stainless steel, rapid grain growth can occur at temperatures higher than 1040 °C,[45] where the temperature is high enough for self-diffusion of Fe as well as the substitutional diffusion of the alloying elements. Given that the bonding temperature during the C-TLP/TG-TLP bonding process in this study well exceeds this critical value, noticeable grain growth was expected. Furthermore, since being a diffusion-controlled process, the growth level is also time dependent. While the isothermal solidification was completed in 120 minutes in the TG-TLP bonding process, a significantly higher holding time was required for the C-TLP bonding scenario, encouraging the grain growth. That is why the mean grain size of the BM after the TG-TLP bonding process (75 μm) was significantly lower than that of the C-TLP-bonded sample (Figures 7(b) and (c)). Moreover, the formation of a secondary phase at the grain boundaries of the austenite grains in the BM of the TG-TLP-bonded sample (Figures 5(b) and 7(c)) can also be another reason behind the slower kinetics of grain growth in this case. This secondary phase is believed to be delta ferrite (δ_{Fe}) due to the high concentration of Cr as a strong ferrite stabilizer and a minor amount of Ni (as the austenite stabilizer element) in this phase, confirmed by the EDS analysis (Table IV). The left-hand endmember of the T–C isopleth in Figure 12(b) shows the equilibrium phases of the AISI 304 stainless steel as a function of temperature, based on which the following transformation takes place at temperatures higher than 1150 °C:

$$\gamma_{\mathrm{Fe}} \rightarrow \gamma_{\mathrm{Fe}} + \delta_{\mathrm{Fe}}. \quad [12]$$

According to the experimental data available in the literature for the AISI 304 stainless steel, the above transformation happens at temperatures higher than 1200 °C,[43] meaning that the Thermo-Calc Software is slightly underestimating this transformation temperature. The C-TLP bonding was performed in a box furnace, and the bonding temperature was kept constant during the process. On the other hand, an induction furnace was used for the TG-TLP bonding, in which the control of the temperature is very tricky, and temperature fluctuations during the process are inevitable. The slight deviation of the temperature to higher than 1200 °C resulted in the formation of the δ_{Fe} during the holding time. Owing to the fact that the TG-TLP sample was air cooled after bonding, the δ_{Fe} cannot fully transform to γ_{Fe}. Residual δ_{Fe} has also been observed in the as-cast AISI 304 stainless steel[43] with cooling rates well below what TG-TLP-bonded samples experienced in this study, confirming the possibility of the presence of δ_{Fe} at room temperature in the BM. It should be highlighted that the BMs in this study were in annealed condition prior to the TLP bonding process. Upon using the TLP bonding process for cold-deformed sheets, the influence of recrystallization on the isothermal

solidification time and the microstructure of the BM should also be investigated.[51]

E. *Mechanical Properties of the TG-TLP-Bonded Specimen*

As the microhardness results in Figure 8(a) revealed, insufficient holding time results in heterogeneity in microstructure and mechanical properties across the joint region. The ASZ and ISZ showed the highest and lowest microhardness values of 230 and 155 HV, respectively. As discussed in Section IV–A, the microstructure of the ASZ in the TG-TLP-bonded sample at room temperature is composed of γ_{Fe} matrix as well as $Cr_2B + M_{23}C_6$ borides and carboborides. By assuming that the $(Cr, Fe)_2B$ has ~ 55 at pct Cr (based on EDS analysis results in Table IV), and the $(Cr, Fe, Mo)_{23}(C, B)_6$ phase is equivalent to $Cr_{23}C_6$, the hardness of these phases should be 2760[52] and 1530 HV,[53] respectively. Therefore, it was expected to obtain higher microhardness values at the ASZ. High-magnification SEM micrographs provided in Figures 3(a) and 5(a) show that the $(Cr, Fe)_2B$ and $(Cr, Fe, Mo)_{23}(C, B)_6$ phases are considerably fine in size. Moreover, a high fraction of γ_{Fe} phase with high toughness exists among these hard and brittle borides/carboborides. These two can justify why the achieved microhardness value for the ASZ is not as high as the values reported in References 52 and 53. Therefore, even when the isothermal solidification is not completed, the joints are expected to show relatively acceptable strength and ductility for some applications. The hardness of the ISZ before the completion of the isothermal solidification (Figure 8(a)) was found to be 16 pct lower than the microhardness of the BM (185 HV). This might be attributable to the lower concentration of alloying elements in the ISZ than in the BM. The microhardness profile across the joint region after the accomplishment of the isothermal solidification is shown in Figure 8(b). As it is evident, both the microhardness of the BM and ISZ has increased to 183 and 215 HV, respectively. The increase in the microhardness of the ISZ at higher bonding times is due to the effective participation of the BM-alloying elements (especially Cr) in the joint region caused by the continuous gap widening during the TG-TLP bonding process. As the EDS map analysis results revealed (Figure 6), a uniform distribution of the Cr, Ni, and Mo was obtained after the completion of the isothermal solidification in the TG-TLP-bonded sample. The increase in the microhardness of the BM can be ascribed to the diffusion of Mo from FM into the BM during the bonding process (Figure 6). Figure 8(b) suggests that the joint region is more uniform after the accomplishment of the isothermal solidification, but still the microhardness of the ISZ is 14 pct lower than that of the BM.

Referring to the engineering shear stress–strain curves and the ultimate shear strength values shown in Figures 8(c) and (d), it can be concluded that the efficiency of the TG-TLP bonding of the AISI 304 stainless steel using Fe–Ni–Mo–B is almost 100 pct. The failure of the bonded specimen from the BM rather than the ISZ (Figure 9(a)) proves that the 14 pct lower microhardness of the ISZ did not adversely affect the shear strength of the joint region. In other words, crack formation and propagation in the BM show that the ISZ was not the preferential failure location. It should also be noted that dimples were observed in the fractured surface (Figure 9(b)), meaning that a ductile fracture mode was dominant. The 100 pct efficiency and high strength of the joint can be attributed to the following:

1. *Non-planar ISZ/BM interface* according to the optical micrographs in Figures 2 and 4, the TG-TLP-bonded samples benefit from a sinusoidal interface. This non-planar interface is formed as a consequence of morphological instability at the solid/liquid interface during the isothermal solidification of the liquid phase caused by the imposed temperature gradient.[36] Such an interface was reported to enhance the strength of the TG-TLP-bonded aluminum alloys[37] (efficiency of 100 pct) by providing mechanical inter-locking between the ISZ and the BM as well as increasing the surface area of the interface. The same findings for AISI 304 stainless steel in this study prove that the sinusoidal interface plays a crucial role in improving the mechanical properties of the TG-TLP-bonded samples.
2. *Application of a Fe-based filler metal with high Cr and Mo contents* although the previous studies in which binary Fe-based or multi-component dissimilar FMs (*e.g.*, Ni-based, Co-based, and pure Cu) were utilized,[28–30,33] a multi-component Fe-based FM was used in this study with high content of Ni and Mo elements, known as effective strengthening alloying elements for iron.[54]
3. *Chemical composition homogenization* by comparing the chemical composition of the ISZ in TG-TLP-bonded sample after completion of the isothermal solidification (Table IV) to that of the as-received BM (Table I), they have almost the same chemical composition. The EDS maps shown in Figure 6 also confirm the uniform distribution of the Cr, Mo, and Ni across the joint region.

Finally, it must be highlighted that the formation of δ_{Fe} in the BM region of the TG-TLP-bonded samples did not play a role in decreasing the joint strength. However, it may have detrimental effects on the corrosion resistance of the joints, especially for high-temperature applications, which needs to be taken into consideration in future studies. One approach to eliminate the chance of the δ_{Fe} formation during the TG-TLP bonding process of AISI 304 stainless steel is to change the bonding temperature so that the system does not enter the two phase ($\gamma_{Fe} + \delta_{Fe}$), even when the temperature fluctuations happen during the bonding process.

V. CONCLUSIONS

In this study, conventional TLP (C-TLP) and temperature-gradient TLP (TG-TLP) bonding of AISI 304 stainless steel were conducted at 1200 °C for different holding times, using a Fe–Ni–Mo–B FM. The following conclusions can be drawn from this study:

- The solidification path of the ASZ in both C-TLP and TG-TLP-bonded samples was investigated by the microstructural observations and Thermo-Calc calculations based on which $\gamma_{Fe} + M_2B$ and $\gamma_{Fe} + Cr_2B + M_{23}C_6$ were proposed to be formed in the ASZ of the respective samples.
- Despite the significantly higher dissolution of the BM during the TG-TLP bonding process and the progress of the isothermal solidification from one of the interfaces, the isothermal solidification time was found to be one third of the C-TLP bonding process (120 minutes in TG-TLP *vs*. 360 minutes in C-TLP bonding).
- Microstructural observations revealed that although the C-TLP-bonded samples possess Cr-rich borides in the DAZ, such precipitates are absent in the TG-TLP-bonded samples. In the case of the TG-TLP bonding process, rapid heating was applied so that the BM/FM/BM system reached the bonding temperature in a few seconds, which is not sufficient for the formation of borides in the DAZ during the melting of the FM and dissolution of the BM.
- The TG-TLP-bonded sample showed a homogeneous chemical composition in the joint region almost equal to the BM composition, eliminating the need for subsequent post-bond heat treatment. The shear strength measurements proved that bonds with parent material shear strength were obtained in the TG-TLP bonding scenario due to the non-linear interface, uniform chemical composition almost the same as the BM, and implementation of a multi-component Fe-based FM with high Ni and Mo contents.

ACKNOWLEDGMENTS

The authors would like to thank Sharif University of Technology's financial support for this research.

CONFLICT OF INTEREST

On behalf of all authors, the corresponding author states that there is no conflict of interest.

REFERENCES

1. W.D. MacDonald and T.W. Eagar: *Annu. Rev. Mater. Sci.*, 1992, vol. 22, pp. 23–46.
2. D.S. Duvall, W.A. Owczarski, and D.F. Paulonis: *Weld. J. (NY)*, 1974, vol. 53, pp. 203–14.
3. A. Ghasemi and M. Pouranvari: *Mater. Des.*, 2019, vol. 182, p. 108008.
4. W.F. Gale and D.A. Butts: *Sci. Technol. Weld. Join.*, 2004, vol. 9, pp. 283–300.
5. D.F. Paulonis, D.S. Duvall, and W.A. Owczarski: Google Patents, 1972.
6. J.C. Barone and R.E. Page: Google Patents, 2009.
7. X. Wu, R.S. Chandel, and H. Li: *J. Mater. Sci.*, 2001, vol. 36, pp. 1539–46.
8. B. Rhee, S. Roh, and D. Kim: *Mater. Trans.*, 2003, vol. 44, pp. 1014–23.
9. X. Yuan, M.B. Kim, and C.Y. Kang: *Metall. Mater. Trans. A*, 2011, vol. 42A, pp. 1310–24.
10. H.M. Hdz-García, A.I. Martinez, R. Muñoz-Arroyo, J.L. Acevedo-Dávila, F. García-Vázquez, and F.A. Reyes-Valdes: *J. Mater. Sci. Technol.*, 2014, vol. 30, pp. 259–62.
11. A. Ghasemi and M. Pouranvari: *Sci. Technol. Weld. Join.*, 2019, vol. 24, pp. 342–51.
12. A. Ghasemi and M. Pouranvari: *Sci. Technol. Weld. Join.*, 2018, vol. 23, pp. 441–48.
13. J.T. Stover: *ERPI*, Palo Alto, CA, 2003, vol. 1005029.
14. Y. Zhou, W.F. Gale, and T.H. North: *Int. Mater. Rev.*, 1995, vol. 40, pp. 181–96.
15. A. Ghasemi and M. Pouranvari: *Metall. Mater. Trans. A*, 2019, vol. 50A, pp. 2235–45.
16. C.W. Sinclair: *J. Phase Equilib.*, 1999, vol. 20, p. 361.
17. C.W. Sinclair, G.R. Purdy, and J.E. Morral: *Metall. Mater. Trans. A*, 2000, vol. 31A, pp. 1187–92.
18. O.J. Adebajo and O.A. Ojo: *Metall. Mater. Trans. A*, 2017, vol. 48A, pp. 26–33.
19. M. Pouranvari, A. Ekrami, and A.H. Kokabi: *Mater. Sci. Eng. A*, 2013, vol. 568, pp. 76–82.
20. S. Şahin and M. Übeyli: *J. Fusion Energy*, 2008, vol. 27, pp. 271–77.
21. A. Bahrami, S.H. Mousavi Anijdan, P. Taheri, and M. Yazdan Mehr: *Eng. Fail. Anal.*, 2018, vol. 90, pp. 397–403.
22. D.J. Kemmenoe, E.A. Theisen, and S.P. Baker: *Metall. Mater. Trans. A*, 2021, vol. 52A, pp. 1–25.
23. D.G.W. Claydon and A. Sugihara: *Report No. 0148-7191*, SAE Technical Paper 1983.
24. M. Hosseini, A. Ghasemi, and M. Pouranvari: *Metall. Mater. Trans. A*, 2020, vol. 51A, pp. 5715–24.
25. Y. Cormier, P. Dupuis, B. Jodoin, and A. Corbeil: *J. Therm. Spray Technol.*, 2016, vol. 25, pp. 170–82.
26. M.A. Balbaa, A. Ghasemi, E. Fereiduni, M.A. Elbestawi, S.D. Jadhav, and J.-P. Kruth: *Addit. Manuf.*, 2020, vol. 37, p. 101630.
27. A. Ghasemi, E. Fereiduni, M. Balbaa, S.D. Jadhav, M. Elbestawi, and S. Habibi: *Addit. Manuf.*, 2021, vol. 46, p. 102145.
28. A. Kazazi and A. Ekrami: *J. Manuf. Process.*, 2019, vol. 42, pp. 131–38.
29. M. Sadeghian, A. Ekrami, and R. Jamshidi: *Sci. Technol. Weld. Join.*, 2017, vol. 22, pp. 666–72.
30. M. Mohammadi and A. Ekrami: *J. Mater. Process. Technol.*, 2020, vol. 275, p. 116276.
31. M.-C. Liu, G.-M. Sheng, H.-J. He, and Y.-J. Jiao: *J. Mater. Process. Technol.*, 2017, vol. 246, pp. 245–51.
32. N.P. Wikstrom, O.A. Ojo, and M.C. Chaturvedi: *Mater. Sci. Eng. A*, 2006, vol. 417, pp. 299–306.
33. N. Di Luozzo, M. Fontana, and B. Arcondo: *J. Mater. Sci.*, 2007, vol. 42, pp. 4044–50.
34. W. Guo, H. Wang, Q. Jia, P. Peng, and Y. Zhu: *High Temp. Mater. Process. (Lond.)*, 2017, vol. 36, pp. 677–82.
35. W. Li, T. Jin, X.F. Sun, Y. Guo, H.R. Guan, and Z.Q. Hu: *Scripta Mater.*, 2003, vol. 48, pp. 1283–88.
36. H. Assadi, A.A. Shirzadi, and E.R. Wallach: *Acta Mater.*, 2001, vol. 49, pp. 31–39.
37. A.A. Shirzadi and E.R. Wallach: *Sci. Technol. Weld. Join.*, 1997, vol. 2, pp. 89–94.
38. M.A. Jabbareh and H. Assadi: *Scripta Mater.*, 2009, vol. 60, pp. 780–82.
39. O.E. Bamidele and O.A. Ojo: *Metall. Mater. Trans. A.*, 2021, vol. 52A, pp. 2261–73.
40. A. Ghobadi Bigvand and O.A. Ojo: *Metall. Mater. Trans. A*, 2014, vol. 45A, pp. 1670–74.

41. A.A. Shirzadi and E.R. Wallach: *Acta Mater.*, 1999, vol. 47, pp. 3551–60.
42. T.L. Yang, T. Aoki, K. Matsumoto, K. Toriyama, A. Horibe, H. Mori, Y. Orii, J.Y. Wu, and C.R. Kao: *Acta Mater.*, 2016, vol. 113, pp. 90–97.
43. S.H. Kim, H.K. Moon, T. Kang, and C.S. Lee: *Mater. Sci. Eng. A*, 2003, vol. 356, pp. 390–98.
44. D. Goldberg and G.R. Belton: *Metall. Mater. Trans. B*, 1974, vol. 5B, pp. 1643–48.
45. J.K. Stanley and A.J. Perrotta: *Metallography*, 1969, vol. 2, pp. 349–62.
46. D.R. Askeland, P.P. Fulay, and W.J. Wright: *The Science and Engineering of Materials*, 6th ed., Springer, New York, 2010.
47. B.H. Armstrong: *Int. J. Thermophys.*, 1992, vol. 13, pp. 489–98.
48. W.F. Gale and E.R. Wallach: *Metall. Trans. A*, 1991, vol. 22, pp. 2451–57.
49. M. Pouranvari, A. Ghasemi, and A. Salmasi: *Metall. Mater. Trans. A*, 2022, vol. 53A, pp. 126–35.
50. P.E. Busby, M.E. Warga, and C. Wells: *JOM*, 1953, vol. 5, pp. 1463–68.
51. A. Nicolaÿ, J.-M. Franchet, J. Cormier, R.E. Logé, G. Fiorucci, J. Fausty, M. Van Der Meer, and N. Bozzolo: *Metall. Mater. Trans. A*, 2021, vol. 52A, pp. 4572–96.
52. J. Lentz, A. Röttger, F. Großwendt, and W. Theisen: *Mater. Des.*, 2018, vol. 156, pp. 113–24.
53. Y. Li, Y. Gao, B. Xiao, T. Min, Y. Yang, S. Ma, and D. Yi: *J. Alloys Compd.*, 2011, vol. 509, pp. 5242–49.
54. J.C. Lippold and D.J. Kotecki: *Welding Metallurgy and Weldability of Stainless Steels*, Wiley, Hoboken, 2005.